

# OVERVIEW ON THE EXPERIMENTAL INVESTIGATIONS OF THE FRACTURE TOUGHNESS IN COMPOSITE MATERIALS

András SZEKRÉNYES\*

Submitted to HEJ. Manuscript no.: MET-020507-A

*This version is for internal use only!*

## Abstract

The experimental determination of the resistance to delamination is very important, since composite materials have superior properties only in the fiber direction. The resistance to delamination is known as the fracture toughness or fracture resistance. To measure the interlaminar fracture toughness of composite materials different kind of specimens and experimental methods are available. The most commonly used *SCB*, *DCB*, *ENF* and *MMB* tests conducted in one- three- and four-point bend fixture are suitable to measure the former quantities. There are several methods for determining the fracture toughness theoretically, experimentally and numerically. The aim of this study is to summarize publications about different experimental investigations of the fracture properties of composite materials. The fracture and damage process can be influenced by many parameters. The investigation of damage in the microstructure of composites requires the usage of optical or scanning electron microscopy. Using these apparatus conclusions can be taken during and after the damage process

Keywords: laminated composite, fracture, fracture toughness, compliance, fracture surface, crack growth, impact

## 1 INTRODUCTION

Laminated composites made of *UD* layers are used for high-performance structural applications because of their high specific strength and stiffness. The composites are anisotropic materials, and have different properties in different directions. The excellent properties of composites can be realized only if the loading direction coincides with the reinforcement direction. In many applications the loading is multidirectional. In these cases delamination, matrix cracking and other type of fracture can occur. The fracture of composite structures are various and widely acknowledged. The interlaminar fracture is commonly encountered in the form of delamination. The delamination or interlaminar cracking is one of the predominant modes of damage in composite structures. The growth of delamination is resulted in stiffness degradation and eventual failure of the composite structure. Delamination can be caused by different type of loading. The resistance to delamination is known as the interlaminar fracture toughness, it is an important composite property and widely acknowledged by designers.

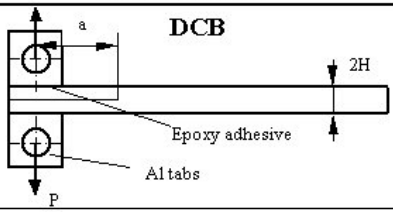
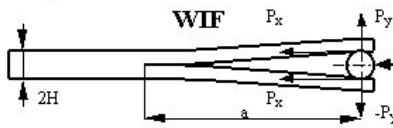
## 2 INTERLAMINAR FRACTURE TOUGHNESS

It became a common practise to characterize the resistance to delamination using fracture mechanics. There is competing terminology in literature, such as fracture toughness, average fracture energy, *J-integral*, *WOF* and critical strain energy release rate. The critical fracture toughness or critical strain energy release rate is the value at the onset of crack propagation. Crack propagation under pure mode-I (opening mode), pure mode-II (shearing or sliding mode) loading has been extensively studied in the

---

\*Department of Applied Mechanics Budapest University of Technology and Economics H-1521 Budapest, Hungary  
Phone: +36 1 463 1170 E-mail: szeki@mm.bme.hu

Figure 1: Specimen design, compliance and interlaminar fracture toughness for mode I loading

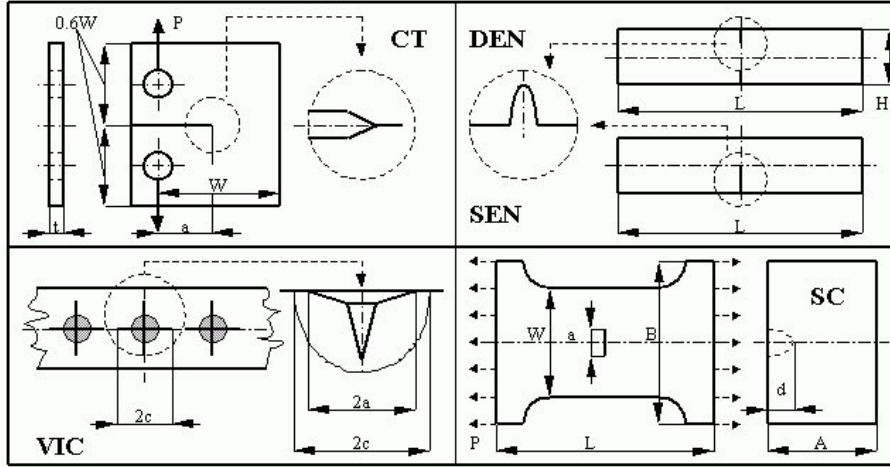
Specimen design	Compliance	Mode I fracture toughness
 <p><b>DCB</b></p> <p>Epoxy adhesive</p> <p>Al tabs</p> <p><math>a</math></p> <p><math>2H</math></p> <p><math>P</math></p>	$C = \frac{8a^3}{WH^3E_x}$	$G_I = \frac{12P^2a^2}{W^2H^3E_x}$ $G_I = \frac{3P\delta}{2Wa}$
 <p><b>WIF</b></p> <p><math>P_x</math></p> <p><math>P_y</math></p> <p><math>P</math></p> <p><math>2H</math></p> <p><math>a</math></p> <p><math>-P_y</math></p>	$C = \frac{8a^3}{WH^3E_x}$	$G_I = \frac{12\left\{\left(P_x r \cos \theta\right)^2 + \left[P_y(a+e)\right]^2\right\}}{W^2H^3E_x}$

literature, but more attention must be paid to mixed-mode I+II loading because it relates to most realistic situations. In fact, composite structures are generally subjected to combinations of mode I and mode II [13]. The contribution of mode III (tearing) fracture to delamination is small in comparison with modes I and II [7]. The critical strain energy release rate is also a common fracture mechanics terminology for the work rate with respect to crack growth [9]. Static and dynamic fracture behaviour of composites has been extensively studied by many authors. Static or dynamic toughness depends on the displacement rate of the crosshead, which loads the specimen. Quasi-static, dynamic and impact tests are intensively applied. The specimen design for mode I loading is depicted in Figs 1 and 2. Measuring mode I fracture toughness the stability of the crack growth depends on the test applied. Crack growth is stable when the specimen with a crack is loaded perpendicularly the fibers. By this method the crack initiation fracture toughness can be measured. In the *DCB* test (Fig.1) the crack growth is stable, the first point is the initiation and the others are the crack growth fracture toughnesses. The characteristics obtained from different tests correspond to each other only if the fracture toughness is independent from the crack length. An increase in fracture toughness is caused by inaccuracy of the *DCB* test due to the effects of shear stresses and fiber bridging in the opposite sides of a crack [2]. The *DCB*, *WIF* [14] and *CT* test [25],[27] for mode I are the accepted methods for measuring the interlaminar fracture toughness ( $G_{IC}$ ). The *WIF* specimen, which is the compression version of the *DCB* specimen is more suitable to investigate the dynamic fracture properties of composites [14]. In Fig.1 the "e" is the correction length. Neglecting the frictional force in the *WIF* specimen the same expression can be obtained as in the *DCB* specimen. The *CT* specimen (Fig.2) is suitable only to investigate the initiation damage due to the insufficient ligament length for further testing [9]. The *DEN*, *SEN* and *SC* specimen (Fig.2) under uniaxial tension measures the mode I fracture

toughness. The *SEN* and *VIC* specimen can be used to characterize also mode I fracture properties in *3PB* or *4PB* setup. The *VIC* specimen (Fig.2) is mainly used in ceramic composites through the *IS* method [29], [32]. The stress intensity around the cracks is used to characterize the fracture properties. The *SENB* specimen is consistent with the *SEN* specimen in *3PB* setup, while the *SENT* is the tensile mode *SEN* specimen. Both specimens measure the mode I fracture properties [17], [30]. The *SEVNB* [11] is similar to the *SEN* specimen but it has V-shaped notch. The mode II fracture toughness is measured by *ENF* (*3PB*), *4ENF* (*4PB*) and *ELS* (*1PB*) specimens according to Fig.3. In the *ENF* specimen

the crack growth is unstable and only one data per specimen can be obtained, initiation fracture toughness can be measured. Applying *4ENF* test, crack growth is stable under displacement control and the complete *R-curve* can be determined from the data of just one test [21]. In contrast, splitting of *UD* specimens with central hole under longitudinal tensile is stable and the entire *R-curve* may be determined [25]. The *R-curve* is the relationship between the fracture toughness and crack length. In many work the *R-curve* behavior, *R-curve* resistance or *J-resistance* [27] were observed, which means that the fracture toughness increases with the crack size, this can be attributed to the fiber-bridging and fiber pullout during the fracture [20], [29]. These fibers increase the resistance to delamination. The *UD* tensile specimen with central hole also determines the mode II dominated fracture and damage properties of composite laminates. Notches and holes occur in many applications of composites and are likely sites

Figure 2: Specimens for mode I loading



of crack initiation and stress concentration, understanding the response in the presence of notches and holes is important in establishing a design methodology for a particular composite. [9] The specimen design for mixed mode I+II loading is depicted in Fig.4. In literature the *SCB*, *DENF*, *MMB*, *MMF* and *CLS* specimens are presented [1]. The *ELS* test can be modified by moving the crack from the mid-plane, this will cause also mixed mode loading [7].

### 3 DETERMINATION OF THE FRACTURE TOUGHNESS

The fracture toughness can be calculated in many ways. In literature the most common is the compliance or compliance calibration method, which assumes linear elastic behavior. Using the compliance method the fracture toughness can be determined as the function of specimen geometry, loading and crack extension. The critical fracture

energy derived from the general *Irwin-Kies* expression [20],[21]:

$$G_C = \frac{p^2}{2W} \cdot \frac{dC(a)}{da} \quad (1)$$

where  $P$  is load,  $C$  compliance,  $W$  is the specimen width and  $a$  is the crack length corresponding to Figs 1,3 and 4. The fracture toughness depends on the specimen geometry and size. Hence the fracture toughness cannot be considered as a material property, but it is a good parameter to investigate the effects of various quantities on the composite toughness. This can be analysed through the fracture energy spent to create an unit area of free surface [4]. The compliance can be computed analytically by use of the classical beam theory. However corrections are necessary in the case of large displacements, shear strain, stiffness effects, etc. [10], [13]. One practical way of taking all these effects into account is to determine the correction length by fitting the experimental compliance [1]. In literature the least-square fitting is very popular [18]. The compliance can be determined as the function of crack length in the case of *UD* composite specimens according to the beam theory [7]. The compliance of the specimen:

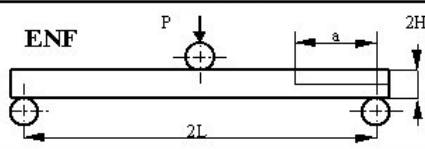
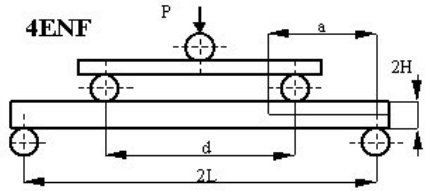
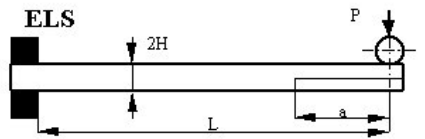
$$C = \frac{\delta}{P} \quad (2)$$

where  $\delta$  is the *COD*. According to the *Castigliano's* principle using the relation between the displacement and the strain energy ( $U$ ) in the case of bending:

$$C = \frac{1}{P} \cdot \frac{dU}{dP} \quad (3)$$

$$U = \frac{1}{2} \int_l \frac{M^2}{IE_x} dx \quad (4)$$

Figure 3: Specimen design, compliance and interlaminar fracture toughness for mode II loading

Specimen design	Compliance	Mode II fracture toughness
 <p><b>ENF</b></p>	$C = \frac{3a^3 + 2L^3}{8WH^3 E_x}$	$G_{II} = \frac{9a^2 P^2}{16W^2 H^3 E_x}$ $G_{II} = \frac{9a^2 P \delta}{2W(3a^3 + 2L^3)}$
 <p><b>4ENF</b></p>	$C = \frac{(9a + 5d - 4L)(L - \frac{d}{2})^2}{8WH^3 E_x}$	$G_{II} = \frac{9(L - d/2)^2 P^2}{16W^2 H^3 E_x}$ $G_{II} = \frac{9P\delta}{2W(9a + 5d - 4L)}$
 <p><b>ELS</b></p>	$C = \frac{3a^3 + L^3}{2EWH^3 E_x}$	$G_{II} = \frac{9a^2 P^2}{4EWH^3 E_x}$ $G_{II} = \frac{9a^2 P \delta}{2W(3a^3 + L^3)}$

where  $M$  is the bending moment as the function of  $x$  and  $E_x$  is the modulus in the fiber direction. The compliance can be determined for modes I and II and mixed mode I+II loading using these equations and the fracture toughness can be obtained as the function of crack length. In Figs 1, 3 and 4 the compliance and the interlaminar fracture toughness for mode I, mode II and mixed mode I+II loading were calculated according to the former procedure. The fracture toughness can be derived as the function of crack length or as the function of  $P$  and  $\delta$ . All the equations were derived

using the classical beam theory considering the specimens as elastic beams. According to the results from Fig.1 the general expression for mode I interlaminar fracture energy [20]:

$$G_{IC} = \frac{nP\delta}{2Wa} \quad (5)$$

where  $n$  can be determined from the slope of the relation between the compliance and crack length. In the case of mode II loading (Fig.3) the compliance is a third order function of the crack length, while the mode II interlaminar fracture toughness depends on the square of the crack length [20], [10]. It must be noticed that applying the *4ENF* procedure the compliance is proportional with the crack length, the fracture toughness is independent of it. The former relation was also proved experimentally [21]. The compliance and fracture toughness for mixed mode I+II loading is depicted in Fig.4. The corresponding quantities for mixed mode I+II loading has similar form than that of the mode II loading. As previously mentioned these expressions have to be completed by other factors, which are dependent of notch geometry, block stiffness, friction, etc. The general experimental compliance laws according to Figs 1,3 and 4 [7], [21]:

$$C = \beta a^m \quad \text{-for mode I loading} \quad (6)$$

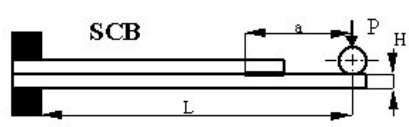
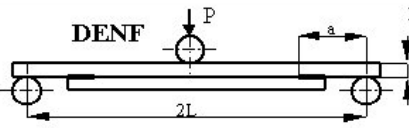
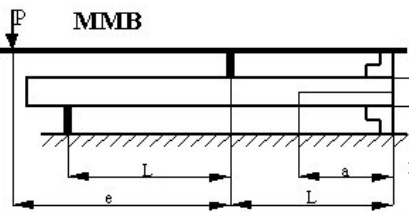
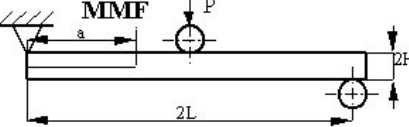
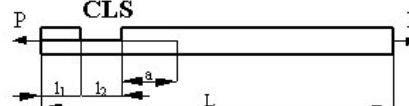
$$C = C_0 + C_1 a + C_2 a^2 + C_3 a^3 \quad \text{-for mode II and mixed mode I+II} \quad (7)$$

The *MCC* method is similar to the compliance method, but the normalized crack length can be derived as the function of compliance ( $C$ ) [14], [24]:

$$\frac{a}{2H} = \alpha \sqrt[3]{CW} + \beta \quad (8)$$

where  $\alpha$  and  $\beta$  can be determined by experimentally measuring the relation between crack length and compliance, hence the mode I interlaminar fracture toughness using the *Irwin-Kies* expression:

Figure 4: Specimen design, compliance and interlaminar fracture toughness for mode I+II loading

<i>Specimen design</i>	<i>Compliance</i>	<i>Mixed mode fracture toughness</i>
 <p><b>SCB</b></p>	$C = \frac{7a^3 + L^3}{2WH^3 E_x}$	$G_{I+II} = \frac{21a^2 P^2}{4W^2 H^3 E_x}$ $G_{I+II} = \frac{21a^2 P \delta}{2W(7a^3 + L^3)}$
 <p><b>DENT</b></p>	$C = \frac{7a^3 + L^3}{4WH^3 E_x}$	$G_{I+II} = \frac{21a^2 P^2}{8W^2 H^3 E_x}$ $G_{I+II} = \frac{21a^2 P \delta}{2W(7a^3 + L^3)}$
 <p><b>MMB</b></p>	$C_I = \frac{8a^3}{WH^3 E_x}$ $C_{II} = \frac{3a^3 + 2L^3}{8WH^3 E_x}$	$G_I = \frac{3a^2 P^2 (3e - L)}{4W^2 H^3 E_x L^2} = \frac{3a^2 P \delta (3e - L)}{8WaL}$ $G_{II} = \frac{9a^2 P^2 (e - L)}{16W^2 H^3 E_x L^2} = \frac{9a^2 P \delta (e - L)}{2WL(3a^3 + 2L^3)}$
 <p><b>MMF</b></p>	$C = \frac{7a^3 + 2L^3}{8WH^3 E_x}$	$G_{I+II} = \frac{21a^2 P^2}{16W^2 H^3 E_x}$ $G_{I+II} = \frac{21a^2 P \delta}{2W(7a^3 + 2L^3)}$
 <p><b>CLS</b></p>	$C = \frac{L + 7a}{2WHE_x}$	$G_{I+II} = \frac{7P^2}{4W^2 HE_x}$ $G_{I+II} = \frac{7P \delta}{2W(L + 7a)}$

$$G_I = \frac{3}{2(2H)} \left( \frac{P}{W} \right)^2 \frac{\sqrt[3]{(CW)^2}}{\alpha} \quad (9)$$

The *MCCI* method is suitable to determine the fracture toughness numerically based on calculating the amount of work required to close the crack [25], [28]. The *MCCI* is very accurate to determine the dynamic energy release rate. The *VCCT* method [23] is consistent with the *MCCI* method. According to this the mode I fracture toughness can be computed for a *FE* model using the above relation:

$$G_I = \frac{1}{\Delta a} [P_{yj}u_{yj-2} + P_{yj+1}u_{yj-1}] \quad (10)$$

$P_{yj}$  and  $P_{yj+1}$  are the forces acting at nodes  $j$  and  $j+1$  respectively and  $u_{yj-1}$  and  $u_{yj-2}$  are the *CODs* at nodes  $j-1$  and  $j-2$  [25], [28]. The  $G_{II}$  also can be calculated by using the load in the  $x$  direction and the components of the *CSD*. The *MVCCT* is also a numerical method connected with *FEA*, the fracture energy [31]:

$$G_C = \frac{1}{2W\delta a} (P_x\delta u + P_y\delta v + P_z\delta w) \quad (11)$$

where  $\delta a$  is the size of the *FEs* around the crack tip as well as the crack extension length,  $P_x$ ,  $P_y$  and  $P_z$  are the nodal force components,  $\delta u$ ,  $\delta v$  and  $\delta w$  are the near-tip displacements under the critical load. The area method is also suitable for determining the fracture toughness [24], [31]. The area between the loading and unloading curves represents the decrease in stored strain energy caused by the delamination crack extension. The mode I critical fracture toughness is obtained by dividing this released energy with the crack area:

$$G_I = \frac{W_i}{A_i} = \frac{(P_i\delta_{i+1} - P_{i+1}\delta_i)}{2B(a_{i+1} - a_i)} \quad (12)$$

where  $P_i$  is the load at  $\delta_i$  displacement (*COD*), and  $P_{i+1}$  and  $\delta_{i+1}$  is the load and displacement after the load drop, respectively. The *WOF* can be defined by the following expression:

$$W = \int P du / dA \quad (13)$$

where  $P$  is the load,  $u$  is load displacement and  $dA$  is the corresponding crack area [28], this integral can be solved by numerical integration, i.e. using the area method.

The *CPT* method is also suitable for calculating the fracture toughness assuming that the deformation e.g. in the *ENF* is pseudo three-dimensional [31]

The *EB* method is another numerical method, based on the energy balance consideration of the whole model considering the strain and kinetic energy [24], [28]. The total energy release rate can be obtained as:

$$G = - \frac{\Delta G_S + \Delta G_K}{\Delta a} \quad (14)$$

where  $\Delta G_S$  is the total strain energy increment,  $\Delta G_K$  is the total kinetic energy increment and  $\Delta a$  is the crack length increment.

The *J-integral* was used by numerous authors to evaluate the fracture energy. The *J-integral* is equivalent with the fracture toughness undergoing small strains under quasi-static conditions. The expression for the *J-integral* [8], [30]:

$$J = \int_g \left( W dy - T_i \frac{\partial u_i}{\partial x} ds \right) \quad (15)$$

where  $g$  is arbitrary contour around the crack tip,  $W$  is the total strain energy density,  $T_i$  are the components of traction vector,  $u_i$  are the components of displacement vector and  $ds$  is the arc length along the contour  $g$ . According to the experimental results of the interlaminar fracture toughness the following relation could be established:  $G_{IC} < G_{IIC} < G_{I+IIC}$  i.e. the mode I fracture toughness is the lowest, while the mixed mode fracture toughness is the highest [20].

## 4 DETERMINATION OF THE STRESS INTENSITY FACTORS

The stress intensity factor is very important property in fracture criteria, it depends on the state of applied load and material configuration. The mode I and II stress intensity factors can be computed [22]:

$$K_I = \sigma_n \sqrt{\pi a} \quad K_{II} = \tau_{n\theta} \sqrt{\pi a} \quad (16)$$

where  $\sigma_n$  is the normal stress perpendicular to the notch,  $\tau_{n\theta}$  is the shear stress parallel to the crack. Completing the former equation:

$$K_I = \sigma_0 \sqrt{\pi a} f(a/w) \quad (17)$$

where  $f(a/w)$  correction factor based on *FEA* results [18]. For the *CT* specimen the mode I stress intensity factor can be expressed as follows [12],[25]:

$$K_I = \frac{P}{HW^{1/2}} f(a/w) \quad (18)$$

where  $P$  is the load,  $a$  is crack length,  $W$  is specimen width and  $H$  is specimen thickness,  $a/w$  is the aspect ratio of the *CT* specimen. In a static formulation of crack problem there is a fixed relation between the stress intensity factor and the strain energy release rate. In dynamic condition, the relation between the  $G$  and  $K$  depends on the crack speed [28]. Considering the former definition [16], [18]:

$$K_C = \sqrt{\frac{EG_C}{(1-\nu^2)}} \quad \text{for plan stress condition} \quad (19)$$

$$K_C = (G_C E)^{1/2} \quad \text{for plan strain condition} \quad (20)$$

Hence in static problems the  $K_C$  is designated as  $G_C$  by some authors. The crack growth rate and the fatigue crack growth rate can be described by the *Paris*-power law [12], [18]:

$$\frac{da}{dt} = A(K_I)^m \quad (21)$$

$$\frac{da}{dN} = B(\Delta G)^d \quad (22)$$

where  $dt$  is the time increment,  $dN$  is the number of cycles increment,  $A, B, d$  and  $m$  are material constants determined from least-squares fitting of the experimental data [18].

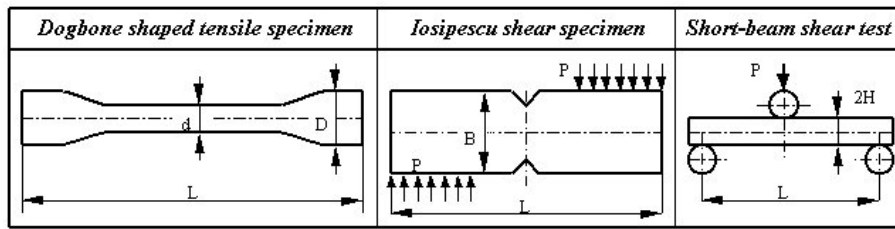
## 5 EXPERIMENTAL RESULTS IN FRACTURE TOUGHNESS IN COMPOSITE MATERIALS

### 5.1 General experimental procedure

Specimens can be manufactured by different types of methods and materials or the combination of composites with other materials (e.g.: *FML*, *CFRML*). The mechanical properties of composite materials can be previously determined, i.e. the tensile strength using dogbone shaped specimen [11], [15], the *ILSS* using the Iosipescu configuration [11], or short-beam shear test setup (Fig.5). In the fracture toughness tests rectangular shape panel has to

be cut from the laminated prepregs. An artificial starter crack or initial delamination can be generated in the specimen, using a non-adhesive *Teflon* or *Al* film to reduce the frictional force. The load can be applied through pins or *Al* blocks bonded to the specimen. *Instron* machine, servo-hydraulic or screw-driven machines [11] can be used to conduct static and quasi-static test with constant cross-head displacement. Dynamic and impact test can be presented by increasing the cross-head displacement rate, or using falling weight impact tower [20], *Charpy* test fixture [16], *SHPB* system [14] or drop-weight impact tester [6]. Test conditions and the tested materials can be varied according to the aim of the investigation. During the loading the specimen fractures, during the test the crack length and

Figure 5: Specimens for the determination of composite elastic constants



load/displacement curves can be measured. The crack length can be measured by visually or using *TM* [11],[12], to measure the surface damage path [9]. The *COD* can be measured by many ways, e.g. using clip gauge [23], [25], *LVDT* [21] or other extensometer [21]. The *CMOD* is the corrected *COD* (e.g. in the *SEN* specimen), assuming the specimen rotated about the centre of rotation located a distance above the crack tip [30]. The fracture process can be followed by video camera and recorder to analyse the crack initiation and propagation [15]. The compliance/deflection curve is generated defining compliance as the ratio of maximum deflection and maximum load for each crack length. The crack length is defined as the mean values of measured on the left and right sides of the specimen during the test. The crack length can be measured by periodically stopping the load. The *SEM* is widespread to examine the microdamages in the specimens [3], [17]. The desired part of the specimen has to be polished and to facilitate the microfailure it is useful to coat the crack surface with gold or palladium [3], [6].

## 5.2 The effects of fiber orientation, laminate and specimen configuration

A study of the fracture behavior and notch sensitivity of a 4 step *3D* braid-reinforced graphite/epoxy composite has been made by FILATOVS and SADLER [9], based on mode I *CT* specimens (Fig.2). The "short" and "long" versions of the *CT* specimen were used, since the "short" specimen is suitable to investigate only the initiation of the damage. The longer specimen, which is a hybrid between the *CT* and the *DCB* specimens was developed to probe the further events. The *WOF* was used and defined by the area (Eq.12) and compliance method (Eq.1). The variation of the failure initiation load as a function of notch-to-braid angle shows increasing failure load as the angle increases, indicating the effect of notch sensitivity. According to the load/displacement curves unstable crack propagation was observed. The *WOF* was determined as a function of crack area. The behavior was divided into three stages. Damage initiation stage showed nearly parallel cleavage with the notch. Propagation stage exhibited multibranching and nucleation of cracking. In the massive damage stage fiber failure occurred. The damage initiating load increases with the notch-to-tow angle. The graph shows the importance of the tow planes as descriptive parameters. Specimens with more fiber tows were tested. Increasing the number of tows less *WOF* is needed and less crack area belongs to a given *WOF*. Reasonable agreement were observed between the area and the compliance method. The *WOF* may be an useful correlative in design methods for textile composites A fracture mechanics study about the impact properties of *PP*-wood flours blends was carried out in [16]. A *MAPP* copolymer was used to increase the dynamic  $K_C$  and  $G_C$  of the material. A virgin *PP* and an *RPP* were used. Notched Izod impact strength test was performed using impact tester. The strength tends to increase with the  $V_p$  in compounds containing *MAPP*, but does the opposite in blends without *MAPP* additive. Considering a fixed *MAPP* content the strength increases with the particle size. The *SEM* evidences micro-voiding and fiber pullout. The impact fracture toughness was studied through *Charpy*-tests. The  $K_C$  and  $G_C$  was determined. The force/time curve of *RPP* shows brittle propagation after crack initiation, the plastic region is much smaller than specimen dimension, the *LEFM* can be used. In the virgin *PP* ductile propagation after the force maximum can be observed, the *PYFM* considering the plastic work dissipation is necessary rather than *LEFM*. The  $G_C$  values of all filled compounds are lower than the neat resin, and the  $G_C$  increases with  $V_p$  in blends with *MAPP*, but decreases slightly when the *MAPP* is absent. The strong interface in the compounds with *MAPP* facilitates the energy-absorbtion through fiber pullout. The  $G_C$  increases monotonously with *MAPP* content in the case of virgin *PP* resin, hence the *MAPP* enhance the fracture energy. The coarser filler should have longer such as fibers, improving the impact resistance. The intralaminar mode I fracture toughness values for a carbon/epoxy cross-ply laminate and its constituent sub-laminates were examined



applying *CT* (Fig.2) specimen and *FEA* in [25]. Specimens with lay-up sequences of  $[0^\circ]_{31} [90^\circ]_{30}$ , and  $[0^\circ/90^\circ]$  were used. Gauge blocks were fixed to the specimen edges to measure *COD*. The tests were conducted with different loading rates. The  $K_{IC}$  values were obtained using Eq.18. A *FE* model was constructed, the  $G_I$  and  $K_{IC}$  were calculated with the *MCCI* method (Eq.10). The variation of *COD* with respect to load is found to be linear for  $[90^\circ]_{30}$ ,  $[0^\circ/90^\circ]$  laminates and for  $[0^\circ]_{30}$  a little nonlinearity is observed. The test and linear *FEA* results shows good agreement within 2-8% for the  $[0^\circ]_{30}$ ,  $[90^\circ]_{30}$ . For the cross-ply laminate the estimated value is 18% more than the tested values. From the fractured specimens there are matrix cracking for  $[0^\circ]_{30}$  and  $[90^\circ]_{30}$  while the cross-ply laminate there is fiber breakage anticipated. The comparison of  $K_{IC}$  also shows good agreement. The theoretical prediction of  $K_{IC}$  shows similar tendency comparing to the test results. According to the results relationship for  $K_{IC}$  of cross-ply specimen based on  $K_{IC}$  of its constituent laminate specimens is established, which shows good agreement with the test and *FEA* data and the values obtained with the *MCCI* method. The *SiC* whiskers have been used as reinforcement to improve the toughness of silicon nitride ceramics. The effects of whisker-oriented alignment (*F*) have been investigated by the *Vickers* indentation method and *R-curve* behavior [29]. For whiskers with completely random orientation  $F = 0$ , for whiskers with unidirectionally preferred alignment  $F = 1$ , so that for a real specimen:  $0 < F < 1$ . Testing bars with different degree of *F* were machined parallel to the direction of *F*, three indentations were produced at the center of the tensile surface of the specimen with a *Vickers* diamond pyramid. *R-curves* were determined measuring the change of *VICs* (Fig.1) in length under *4PB* tests, the three indentations were in the inner span. The crack length was measured, the  $K_I$  was calculated. *R-curves* shows the *F* improves the hardness and resistance to damage of *SiC/Si<sub>3</sub>N<sub>4</sub>* composites. The *SiC/Si<sub>3</sub>N<sub>4</sub>* composite with initial crack length at a higher degree of *F* has high resistance to damage under loading. Whisker bridging and pullout behind the crack tip are considered as main contributions to increased fracture toughness. Micrographs also indicate that the orientation of whisker clearly influences the process of whisker toughening. The experimental investigation of the mode I fracture toughness of *IPCs* (*420* stainless-steel/bronze, *316L* stainless-steel/polymer) was carried out in [30]. *SENB* (Fig.1) specimens in *3PB* setup were used. Except for the *420 IPC* all specimens exhibited stable crack growth. Load-line displacement were measured using an *LVDT*\*. *420* specimens were measured by monotonically increasing the *COD*. Crack length was measured by an *OM*, the compliance method were used (Eq.1), *J-resistance* curves were determined by fitting. Stable crack growth were observed in all specimen. In the *420* specimen the *J-integral* is larger in lower volume fraction, in the *316L* specimen it was higher in larger stainless content. *SEM* evidences secondary cracking, large deformations and plasticity. The crack seems preferring to travel along phase interfaces, crossing the stainless phase only at sintered joints. In the *316L* the interfacial bond is weak and provide little resistance to crack growth. Crack bridging by the ligaments of stainless was observed. In the *420* specimen the final crack extension was not predicted accurately and crack tunneling was observed. For both *IPCs* the *R-curve* behavior was explained by crack bridging and development of a process zone comprising plasticity and secondary cracking in regions away from the primary crack. For the *420* specimen the bronze is more ductile and provide the resistance to crack growth. For the *316L* specimen the interconnectivity of stainless forces the crack to be intercepted by a ductile phase, increasing the resistance to crack growth.

The identification and forecast of delamination in carbon/epoxy laminates was investigated by ALLIX et al. [1]. The laminates were modeled as a stacking sequence of damageable layers and *2D* interlaminar interfaces. Links between damage and fracture mechanics were developed using the mode I, II, III and the total critical-energy release rates. *DCB* (Fig.1), *ENF* (Fig.3), *MMF* and *CLS* (Fig.4) tests were conducted on  $[(+\theta/-\theta)_{4S}/(-\theta/+\theta)_{4S}]$  laminates with  $\theta = 0^\circ, 22.5^\circ$  and  $45^\circ$ . The rates were corrected by the experimental compliance calibration for the *DCB* and *MMF* tests. The highest  $G_C$  values were observed in the *ENF* specimens. The  $G_C$  increases with  $\theta$ , this can be associated with the fiber bridging. The energy dissipated inside the layers was accounted correcting the mean critical-energy release rate, resulted that the  $G_C$  in the  $0^\circ/0^\circ$  interface was always lower than before the correction, the parameters of the interface model were identified. The initiation of the delamination was studied. The initiation strain were measured for all values of  $\theta$ . Brutal rupture occurred in the  $\theta = 22.5^\circ$ -ply-based laminate. The delamination initiation were simulated and the strains were obtained. The predictions are not very close to the experiments due to the damage inside the layers was not accounted, but the location of delamination was obtained exactly.

### 5.3 Fracture toughness of fiber/metal laminates

LAWCOCK et al. investigated the effects of adhesion bonding between *Al* sheets and composite prepreg on the mechanical property profiles of *CFRMLs* [15]. The composite layer was sandwiched between two *Al* sheets. Two different surface preparation methods were applied, method I involved hand abrasion, method II used a coupling agent to improve adhesion. *DCB* test (Fig.1) for the *CFRML* were conducted. Stable crack growth were observed for both specimen. The initiation  $G_{IC}$  was much larger in specimens prepared with method II than specimens prepared with method I. In method I the crack propagation was along the interface between the composite and the *Al* adherend, resulting in an almost constant  $G_{IC}$ . Specimens with method II produced *R-curve* effect due to fiber bridging. It is concluded that method II produces a stronger bonding. Tensile strength and *ILSS* were determined, the latter using *3PB* and *5PB* fixture (Fig.5). No substantial differences were found in the strength and stiffness, but the *ILSS* is slightly reduced in the case of method I. To evaluate residual strength specimens with central saw-cuts or circular holes with various sizes were also used. For both surface treatment, increasing the size of the saw-cut and the central hole the residual strength decreases, but it is almost unaffected by the surface treatment. In the presence of saw-cut delamination prior to fracture, in the case of central hole plastic yielding in the *Al* layer with delamination is observed, the delamination area was larger in specimens treated with method I. The residual strength of notched *CFRMLs* is governed by the crack initiation and growth in the composite layer.

REYES et al. investigated the quasi-static and impact properties of a novel *FML* (*Al*/composite) system based on a *GFPP* [20]. The  $G_{IC}$ ,  $G_{IIC}$ ,  $G_{I+IIC}$  were determined by the compliance method (Eq.1) using the *DCB* (Fig.1), *ENF* (Fig.3) and *SCB*, *DENF* (Fig.4) geometries with different laminate configuration. The *SCB* specimen were loaded with different displacement rates. The failure mechanism at the onset of fracture were elucidated using the *DENF* specimen with different displacement rates. According to the tensile tests the tensile modulus of the composite decreases with increasing the  $V_f$ , and increases with increasing the  $V_f$  in the case of laminates. The *SCB* tests were conducted with different stacking sequences, the crack advanced in small steps. The fracture energy rises rapidly with increasing crack length until the interfacial fracture toughness is reached. The interfacial fracture toughness varies with the displacement rate, the fracture toughness is depending on the location of the primary crack. *LVI* tests were conducted using samples with different stacking sequences and applied impact energies. The upper ply was always *Al* one, secondary impacts were avoided. The residual tensile strength was determined removing these tested samples. *SEM* shows permanent damage around the point of impact and large number of micro-cracks in the matrix. These cracks can extend along and around the fiber/matrix interface. The composite ply significantly contributes to the energy-absorbing process, the composite/*Al* adhesion remains impressive. The damage area increases with increasing the impact energy. A different percent of strength reduction can be observed increasing the impact energy. Thermoplastic based *FMLs* exhibit excellence resistance to impact loading.

### 5.4 The effects of measuring techniques and data reduction schemes

An experimental study to investigate the accuracy of the  $\frac{1}{4}$ *ENF* (Fig.3) test for the determination of mode II delamination toughness was conducted by SCHUECKER and DAVIDSON [21]. It has been observed that the  $\frac{1}{4}$ *ENF* test gave values 8-20% higher than the *ENF* (Fig.3) test, the difference increases with increasing the ratio of the inner span versus the outer one. The error might be due to the inexact measuring techniques for determining crack length and compliance.  $\frac{1}{4}$ *ENF* and *ENF* tests were conducted on *UD* carbon/epoxy specimens with different span ratio and results were compared. The compliance calibration method (Eq.1) was used. Initiation and propagation tests were conducted. The crack length was measured visually, using c-scan system and *LVDT*. The specimen deflection was determined from the testing machine's actuator displacement and from the average of two *LVDT* readings. The data from  $\frac{1}{4}$ *ENF* tests may be reduced to produce eight different  $G_{IIC}$  values. *ENF* initiation tests were also performed using similar apparatus. In the  $\frac{1}{4}$ *ENF* test the C/crack length curve was linear, in the *ENF* test it was fit with a third order polynomial. Initiation results show the  $\frac{1}{4}$ *ENF* test gives 2-12% higher values than that of the *ENF* test. In the  $\frac{1}{4}$ *ENF* test the biggest difference in  $G_{IIC}$  is observed between the visual and c-scan method. According to the  $\frac{1}{4}$ *ENF* propagation test the propagation toughness is 20-30% higher than the initiation one. If compliance and crack length are measured accurately the  $\frac{1}{4}$ *ENF* and *ENF* tests will essentially produce the same toughness values. It is recommended that the compliance in  $\frac{1}{4}$ *ENF* test be determined from the load/deflection curve.

The mode II fracture behavior of graphite/epoxy multidirectional laminates was studied by YANG and SUN using three data reduction methods [31]. *ENF* (Fig.3) specimens with layup of  $[0_{10}/90/0_9/0//\theta/0_9/90/0_{10}]$  were used, the interface indicated by // was at the mid-plane of the laminate,  $\theta$  was varied in the range from 0 to 90°. The *ENF* test were performed, an  $a/L$  ratio was selected to assure stable crack extension during the precracking process, the crack tips were located using *OM*. The load/deflection curve was recorded by a *PC*. In the case of unstable crack extension the load has a sudden drop right after the delamination initiates. Considering the stable case the load capacity gradually increases as the delamination grows. The total strain energy release rate was obtained by the area method (Eq.12), the *CPT* and *MVCCT* (Eq.11). The effects of various parameters on the  $G_{II}$  of  $0/\theta$  interfaces were examined. The effects of overhang, span and specimen width can be neglected. Examining different fiber orientations the fracture toughness approximately remains constant. Similar results can be observed examining the effects of initial crack length and friction. The highest  $G_{II}$  values were obtained from the area method, the *MVCCT* gave much lower values. The lowest  $G_{II}$  values can be calculated using the *CPT*. These results show  $G_{II}$  values depend on the data reduction method used.

## 5.5 The effects of temperature on the interlaminar fracture toughness

CELEMIN and LLORCA presented a study in which, the mechanical properties of  $Al_2O_3/Nicalon\ SiC$  composite were measured at ambient, intermediate and elevated temperatures [4]. The mode I fracture test were carried out by *3PB* of notched bi-directional  $[0^\circ/90^\circ]$  prismatic bars, placed in a furnace to test at elevated temperature. The crosshead displacement were monitored through an *LVD*. Significant decrease in the tensile strength and modulus were observed increasing the temperature. The nominal fracture toughness and the fracture energy decreased significantly from ambient to 800°C, and remained constant above this temperature. According to the *SEM* the average fiber pullout length in the specimens tested at 1000 and 1200°C was shorter than in those tested at 25°C. The fraction of fibers broken in the matrix crack plane was maximal at 800°C. The fiber strength and interfacial sliding resistance were estimated as a function of temperature through quantitative microscopy techniques. Both parameters remained constant up to 800°C, but decreased rapidly above this temperature. The composite strength were computed based on the assumption of global load redistribution takes place when fiber fracture occurs. The theoretical results are in good agreement with the experiments. The fracture energy were calculated based on the results of microscopy techniques. At 25°C the experiments agreed well with the model predictions, the damage zone propagated containing multiple cracks. At high temperature failure was localized around one single crack.

The thermal and mode I fracture behavior of three  $Al_2O_3 - SiC_w$  composites and  $Al_2O_3$  have been investigated in [5]. Composites, designated as *A30R*, *A30T* and *A30B* were manufactured. The "R" and "T" *SiC* grades were well-defined whiskers with mean diameter of  $0,3 - 0,7\mu m$ , while the "B" grade material was coarser and more variable with mean diameter of  $1 - 2\mu m$ . The thermal conductivity decreases increasing the temperature. The mode I fracture toughness of the composites was evaluated from the stress intensity of the *VICs* (Fig.2). The indentation load was varied. The crack was assumed to stop when the stress intensity at the crack tip equals to the fracture toughness of the material. All composites exhibited higher fracture toughness values than the  $Al_2O_3$ . The *A30R* composite exhibited *R-curve* behavior. The thermal shock resistance was also measured. Precracks were made with a *Vickers*-indenter. The crack length- $\Delta T$  curve can be divided into three regimes. At low  $\Delta T$  no significant crack growth can be observed. In medium  $\Delta T$  interval stable crack growth occurred. At certain values of  $\Delta T$ , some of the cracks grow unstably. The ranking of the composites and the  $Al_2O_3$  according to thermal shock resistance agrees well with the ranking according to fracture toughness, but disagrees with the ranking according to thermal conductivity. These experiments indicates that the fracture toughness is very important in defining the thermal shock resistance.

An experimental and analytical investigation in cryogenic mode I interlaminar fracture behavior and toughness of *SL-E* woven glass-epoxy laminates was conducted in [24]. The *DCB* (Fig.1) tests were performed with varied specimen lengths at *RT*, 4K and 77K. Low temperature environments were achieved by immersing the loading fixture and specimen in liquid *N* or *He*. Several  $G_I$  values for each specimen were obtained. The fracture toughness was determined using the *MCC* (Eq.8) and the area method (Eq.12). At *RT* and 77K the  $G_I$ /crack length curves show, the  $G_{IC}$  are approximately constant in the crack length. The area method gives lower values than the *MCC* method. The load-displacement curve of 4K is similar to that of 77K, but it provides lower values. Stable crack growth occurred at *RT*, at 77 and 4K the crack growth was unstable. No significant differences were observed between the values obtained

by the *MCC* and the area method at *RT*. A *3D FEA* using the quarter of the *DCB* was carried out. The energy release rate was evaluated by the global energy method. The *FEA* result averages about 25% lower than the area method result at *RT*. At cryogenic temperature the *MCC* overestimates the  $G_{IC}$ , but there is a good agreement between the results of the area and the *MCC* method. According to *SEM*, the crack generally progresses at the fiber-matrix interface. The dominant failure mode at cryogenic temperatures is interfacial failure.

The processing and mechanical properties of  $Al_2O_3/Ni_3Al$  *IPCs* was presented by SKIRL et al. [26]. Composites with Ni3Al contents of 15% to 30% were examined.  $Al_2O_3/Ni_3Al$  and  $Al_2O_3/Al$  composites were investigated experimentally. Strength measurements were made using rectangular specimens in *4PB* for each microstructure at *RT*. High temperature mechanical testing were performed between 600°C and 1000°C. At *RT* and 800°C the strength was approximately constant against the content, but above the content value of 30% strength is dramatically increased. The fracture strength of composite with 20% content was constant against the temperature. Fracture toughness ( $K_{IC}$ ) was measured with the same equipment using *SEVNB* specimen. At *RT* the fracture toughness increased almost linearly with the content of metal. At elevated temperature the composite exhibits lowest values of fracture toughness. The fracture toughness of composite with content of 20% decreases with temperature. *SEM* shows debonding between the ceramic and  $Ni_3Al$ . The Young moduli were also measured, calculated with the rule of mixtures and another special theory. Experimental values clearly differ from the formers, the moduli of composites only with content of 30% corresponds to the theoretically estimated value.

The mechanical properties of  $SiC-Mo_5(Si, Al)_3C$  composites with infiltrated phase were investigated and compared with *RB-SiC* and *SiC/MoSi<sub>2</sub>* composites by ZHU and SHOBU [32]. Fracture strength and toughness were measured experimentally up to 1600°C. The fracture strength was determined applying *3PB* test. The average *RT* flexural strength and the standard deviation are similar and in the same interval in all the three types of composites. A significant increase in the strength can be observed between 1200 and 1600°C. The behavior is linear up to 1200°C and plastic deformation is observed at  $\geq 1400^\circ C$ . The  $SiC - Mo_5(SiAl)_3C$  composite has superior strength over the *RB-SiC* composite in the range of 1400 – 1600°C. The fracture toughness were determined by the *IS* method using the same equipment. The indentation was made by a *Vickers*-indenter. The fracture was initiated from the indent. The fracture toughness significantly increases at elevated temperatures, it was mainly attributed to the plastic deformation of the infiltrated phase of the composites. The influence of annealing in air was also studied and dramatic increase was observed in the fracture toughness.

## 5.6 The effects of loading rate, strain rate and crack speed

The effect of matrix toughness and loading rate on the mode II interlaminar fracture toughness was investigated by COMPSTON et al. [6]. Glass-fiber/vinyl-ester laminates were tested using *ENF* (Fig.3) specimens. Brittle and rubber-toughened vinyl-ester matrices were used. Load-displacement plots were recorded as a function of time. Static (1, 10, 100, 1000mm/s) and dynamic (impact, 3m/s) tests were conducted varying the displacement rate. The  $G_{IIC}$  was determined from the compliance method (Eq.1). The load-displacement profiles (1000mm/min) are similar for the specimens, unstable fracture occurred at the maximum load point, designated as the nonlinear point. In the case of 3m/s similar loading condition to a static test can be observed. An inflection point in the displacement-time curve indicates the crack initiation ( $G_{IIC} - init$ ). The specimen fracture surfaces were investigated by *SEM* and OM. Results show no significant rate effect on the  $G_{IIC}$ . Micrographs were made with rate of 1mm/min and 3m/s and it was concluded that there is no effect of matrix toughness on  $G_{IIC}$ . This can be explained by the suggestion, that the mode II failure is controlled by the interface that has dominant role in the failure process. According to previous publications, friction is significant in thicker specimens. However COMPSTON et al. reported no influence of thickness.

FRACASSO et al. investigated the effects of strain-rate on the mode I and II fracture toughness of interleaved carbon/*PEEK* composites [10]. *UD* and woven fabric laminates were investigated, tests were carried out using the *DCB* (Fig.1) and *ENF* (Fig.2) tests. For the *UD* composite crack propagation was stable for both modes and took place at a crack speed, approximately constant during the test. No evidence of a crack resistance was observed. Delamination was mainly controlled by the competition between matrix cracking and interfacial debonding. In the *UD* composite for mode I failure, *SEM* micrographs show debonding is the dominant fracture mechanism. For mode II, no debonding was observed, fracture is controlled by plastic deformation of the matrix. Fracture toughness values increase with interleaving thickness. The  $G_{IC}$  is strongly dependent on the crack speed,  $G_{IIC}$  only slightly varies

with the speed. In the woven fabric composites unstable crack growth was observed. The  $G_{IC}$  shows higher values than that of the  $UD$  composite. Plastic deformation of  $PEEK$ -rich regions at fiber crossing is shown by micrographs. The  $G_{IC}$  shows the same dependence as observed in the  $UD$  composite. Interleaving with the same matrix resin increase the delamination resistance and has proved to be a viable technique of toughening. The delamination toughness of the composite is controlled by the rate dependence of the resin toughness.

The rate dependence of mode I fracture behavior in  $UD$  carbon/epoxy laminates has been investigated by KUSAKA et al.[14].  $DCB$  (Fig.1) specimens were used for quasi-static tests, the  $WIF$  (Fig.1) method was employed to conduct the impact tests. A strain gage was used to measure the surface strain, the  $G_{IC}$  was determined by measuring the critical values of the strain and the crack length. The time derivative of the energy release rate was denoted as loading rate. The loading rate/ $G_{IC}$  curve shows three distinct regions. At low loading rate (region I) unstable crack growth can be observed at fracture initiation. The  $G_{IC}$  decreases stepwise in the rate-sensitive transition region (region II). The decreasing of  $G_{IC}$  is followed by region III, where stable crack growth was observed at higher loading rate. In the  $DCB$  test in region I unstable crack propagation, in region III stable crack growth was observed. The crack growth behavior was modeled incorporating the rate dependence of  $G_{IC}$  and the contribution of the kinetic energy. The agreement between the model and experiments was reasonable. The crack arrest toughness and crack velocity was obtained numerically and both are in good agreement with the experiments.  $SEM$  shows two distinct areas in regions I and II with matrix failure and debonding. Whitening in first area shows unstable fracture, in the second area dark region corresponds to the unstable crack growth. Smooth fracture surface was observed in region III with similar failure mechanisms.

A modified  $ENF$  specimen was used by TSAI et al. to determine the mode II dominated dynamic fracture toughness at high propagation speeds [28].  $UD$  glass/epoxy and carbon/epoxy specimens were used. The crack extension history curve was used as input for the  $FEA$ . Crack surfaces were bonded by interface elements with zero thickness. Crack propagation was modeled by separating the nodes. The energy release rate was calculated at the end of each step by the  $MCCI$  (Eq.10) and the  $EB$  (Eq.14) method. The dynamic  $G_{II}$  was not affected by the variation in the crack speed history. It is shown that the dynamic  $G_{II}$  is approximately the same as the static  $G_{II}$  calculated from the conventional  $ENF$  test within 300-700m/s, but for lower crack speeds the dynamic  $G_{II}$  is significantly higher than the static one. The mixed mode crack propagation was also studied using the modified  $ENF$  test. The precrack was moved from the midplane and a small pin was inserted into the crack. In the  $FE$  model the precrack was opened with the displacement equal to the diameter of the pin. Using four specimens the critical energy release rate was plotted against the crack speed. In comparison similar  $ENF$  specimens with no adhesive were tested, the quasi-static critical energy release rate was estimated with the area method (Eq.12). It is found that the dynamic fracture toughness does not seem to deviate from the static fracture toughness up to 1100m/s displacement rate

## 5.7 The effects of acidic environment, elevated pressure and cyclic loading

The effects of acidic stress environment on the stress intensity factor for  $GRP$  laminates was investigated by KAWADA and SRIVASTADA [12].  $E-VE$ ,  $E-ER$  and  $C-VE$   $CT$  (Fig.2) specimens were used with the stacking sequence of  $[0^\circ/90]$  and were exposed in  $HCl$  acid of various concentration and temperature. Constant tensile loading was applied, the crack length was measured by a  $TM$ . The rate of crack propagation was determined. The  $K_I$  was calculated using Eq.18. The trend in acidic behavior is divided into two regions according to the crack propagation rate/ $K_I$  relation. First the crack propagation is converged where crack growth proceeds on a single plane, then stable crack propagation region is observed according to the Paris-power law (Eq.21), the stress corrosion leads to fiber pullout and roughening of the fracture surface. The rate of crack propagation increased with temperature and concentration of acid. The  $C-VE$  composite behaves similarly to the  $E-VE$ , but the corrosive resistance of the  $C-VE$  is higher, so that the  $K_I$  of  $C-VE$  is greater than that of the  $E-VE$  composite. Micrographs show that the  $E-VE$  composite fractured very easily in both stages. However the  $E-VE$  composite has higher corrosive resistance than the  $E-ER$ . The  $C-VE$  composite is suggested to be used in stress corrosion conditions with high temperature, because it exhibits higher  $K_I$  than the  $E-VE$  and the  $E-ER$  composite.

The effects of pressure on the fracture behavior of rubbery particulate composite were investigated by MILLER and LIU [18].  $SENT$  and  $SC$  (Fig.2) specimens were used. The test were conducted in a pressure chamber and crack growth in both the  $SENT$  and  $SC$  specimens, growth rate only in the  $SENT$  specimens were examined. The process were followed by a video camera. In the  $SC$  specimen

only crack width was measured. For the *SENT* specimens *FEA* was conducted to obtain stress intensities in each data point. The  $K_I$  was determined based on the *J-integral*. The initiation fracture toughness was defined as the stress intensity at the given point in the time, when crack growth first occurs. The overall initiation fracture toughness of the *SENT* specimen was determined using a regression plot at ambient and elevated pressure. No thickness effect on the fracture toughness was observed, so plane strain condition is apparent. The effect of pressure is to increase the  $K_C$  value by a factor of about 2. The crack growth rate was determined by the *Paris*-power law (Eq.22). The crack speeds were obtained by fitting a polynomial curve into the points of each data set and using the derivatives. The constants of the power law then were obtained from these curves. The pressure increase the initiation fracture toughness and slows the void nucleation and growth in the composite.

Delamination fatigue-crack growth experiments have been carried out on *UD* glass/epoxy composite by KENANE and BENZEGGAGH [13]. The *DCB*, *ELS* (Fig.3) and *MMB* (Fig.4) specimens were used, to study the mode I and II and the mixed mode I+II loading. The total critical strain energy release rate (GTC) was determined. The delamination crack growth rate ( $da/dN$ ) was predicted through the *Paris*-power law (Eq.22). During the test,  $G_{max}$ ,  $G_{min}$  and  $da/dN$  were monitored. The mode ratio  $G_{II}/G_T$  was determined according to equations. Crack length/number of cycles relations show that the crack propagation is relatively unstable for high mode ratios but is stable for low mode ratios. The propagation in mode II was unstable, in mode I it was stable. The measured crack growth rate data was correlated with the corresponding strain-energy release rate. The  $G_{II}/G_T$  ratio was varied from 0 to 100%, in each investigated mode ratio the results were fitted to the *Paris*-power law. The coefficients of the power law ( $d, B$ ) were determined by least-squares fitting of the  $\Delta G - da/dN$  curves. If  $G_{II}/G_T = 0$ , then pure mode I loading, if  $G_{II}/G_T = 1$ , then pure mode II loading exists. Finally a semi-empirical mixed-mode fatigue criterion was proposed to predict the coefficients of the *Paris*-power law. The agreement between experiments and predictions was excellent, but to validate results it would be desired to study composites with different matrices and interfaces.

## 5.8 The effects of shear damage, fiber pullout and debonding damage

The notch sensitivity of *CP-CC* laminates and *QI-CC* laminates were investigated in [11]. From the tensile test the measured stress/strain relation was almost linear up to the final fracture in both *CC*, but the *CP-CC* has higher elastic modulus. The shear test were made according to the Iosipescu configuration (Fig.5). The *QI-CC* has almost linear shear stress/strain relation up to the ultimate fracture, while the *CP-CC* exhibited strong nonlinear deformation. The fracture toughness test was presented using *DEN* specimen (Fig.2) with varying the notch-root radius to change the level of stress concentration. The fracture behavior of *CCs* was profoundly not affected by the shear damage, shear nonlinear deformation and the *CCs* are not sensitive to the intensity of stress concentration but are sensitive to the specimen dimension. The fracture resistance was examined using *CT* specimen (Fig.2) and the compliance method (Eq.1). The *R-curves* of both materials almost coincided. A *FEA* of the *DEN* specimen was conducted under plane-stress conditions, the shear modulus degradation was considered. The effect of shear nonlinearity on the stress distribution is negligibly small to explain the *R-curve* behavior. The shear damage cannot sufficiently contribute to the large stress relaxation to explain the high fracture toughness of the *CCs*. The fracture of the notched specimens can be described by the *R-curve* concept, and the source of the *R-curve* is the strength-enhancing behavior, that is caused by microfractures

The in-plane fracture resistance of a *FM* was investigated by MCNULTHY et al. [17]. The importance of fiber pullout was demonstrated by experiments. The tests were performed on a *Si - 3N<sub>4</sub>/BN FM* with  $[0^\circ/90^\circ]$  and  $\pm 45^\circ$ . The fracture resistance were measured using *SEN* (Fig.2) specimen in *3PB* test. The *WOF* was calculated using the area method (Eq.12). Stable crack growth was observed. The stress-*CMOD*, compliance-*CMOD* curves were obtained by experiments and by *LEFM*, and the correlation between them found to be poor. The fracture resistance curve of the  $[0^\circ/90^\circ]$  specimen firstly increase discontinuously at a given level, then it increases almost linearly with crack length. Unnotched specimens were tested in a *4PB* fixture to estimate the Young's moduli and unnotched strength. The fracture resistance of the monolithic *Si<sub>3</sub>N<sub>4</sub>* was measured using chevron-notched flexure specimens. Initial crack growth occurred unstably and load drop occurred. The fiber pullout length were measured from a series of *SEM* micrographs ( $[0^\circ/90^\circ]$  specimens). The form of the bridging law was determined based on a micromechanical model of fiber pullout, and based on the load-*CMOD* response of *FM* specimens following fracture of all fibers. Both approaches indicate the bridging law follows an exponential form characterized by the strength and fiber pullout length, decreasing with increasing *COD*. The law were

used to simulate the load-*CMOD* response during cracking of the fibers. The load-*CMOD* response of  $[0^\circ/90]$  and  $\pm 45^\circ$  specimens can be simulated more or less accurately, but larger discrepancies between experiment and theory can be observed in the former.

TOHGO et al. presented a study about the fracture toughness of *Nylon 66* composites [27]. The glass particles were used with and without surface treatment. Tensile and fracture toughness tests were carried out by the dogbone shaped (Fig.5) and *CT* specimen (Fig.2). The stress/strain response shows the interface-treated composite was strengthened by the particles but the conventional (untreated interface) composite was weakened by them. The Young's moduli increases with the  $V_p$  in both composites. The tensile strength decreases with the  $V_p$  in the interface-untreated composite. The interface-treated composite possess higher tensile strength increasing the  $V_p$ . The J-resistance curves and the tearing modulus ( $dJ/da$ ) were determined. Increasing the  $V_p$  the fracture toughness increased in the conventional composites, and decreased up to 10% and then slightly increased in the interface treated composites. Increasing the  $V_p$  the tearing modulus decreased in both composites. In the *FEA* (plain strain condition) the matrix was modeled as elastic-plastic material and the progressive debonding damage of the particles from the matrix was considered. Debonding parameters were determined. The tensile strength is enhanced by the particles and reduced by the debonding damage. On the crack-tip field due to the stress concentration crack initiation and growth resistance is reduced by the particles, the debonding damage acts as a toughening mechanism. Micrographs showed that the damage mode of both composites was interfacial debonding, but in the interface-treated composite the debonding damage was reduced due to high interfacial strength.

## 5.9 Specimens with central crack, effects of hole diameter and crack angle

Splitting of *UD* aramid, glass and carbon fiber-reinforced composites with open hole was studied by BAZHENOV [2]. *UD* ring specimens were used, a cylindrical hole was drilled in the center of the ring. The tensile stress was uniform along the length of the ring. The split length near the hole was measured, the  $G_{IIC}$  was determined. The compliance was obtained as the sum of the compliances of the zones of uniform, nonuniform stress distribution and the splitting zone. The critical splitting stress decreases as the square root of the hole diameter. The split length increases with the applied tensile stress, split growth was stable after their initiation. The glass/epoxy composite exhibited the lower split length values. The  $G_{IIC}$  increases with the split length, depending on the fiber type. The *R-curve* behavior is explained by the bridging of unbroken fibers and by friction of the opposite sides of the split as the *SEM* observations proved previously. The stress in the strain gages, glued to near and far from the hole was not equal to zero after split tips have passed the back edge of the gauge, proving the existence of shear stresses. It was observed that the splitting stress decreases as the hole diameter increases. On the other hand some increase in  $G_{IIC}$  with an increase in the diameter was obtained. This can be explained by the breakage of bridging fibers. The  $G_{IIC}$  decreases monotonically with the  $V_f$  for all composites. Finally the  $G_{IIC}$  tends to increase with the curing temperature of the matrix, showing the effectiveness of the matrix properties on the  $G_{IIC}$ .

BELMONTE and coworkers investigated the notched tensile fracture of *QI*  $[0^\circ/90^\circ/+45^\circ/-45^\circ]_S$  and  $[90^\circ/0^\circ/+45^\circ/-45^\circ]_S$  woven fabric E-glass/epoxy laminates [3]. Tensile and *SEN* (Fig.2) tests were done. The Young-modulus and the unnotched strength were determined. In the notched specimens central holes were drilled with different diameter. The strength decreases against the ratio of notch size/coupon width. The  $G_{IC}$  was measured by the *SEN* test, and calculated by the compliance method (Eq.1). The average  $G_C$  and  $K_C$  of the laminates were determined. The notched coupons were loaded just below the failure load, unloaded, then the region was viewed with *SEM*. The initial failure was matrix cracking, damage zone formed at the notch edge in both sides of the hole. These critical damage zones were modeled as a rectangle and were described by their width and length separately in both sides. Both the length and width are constants against the notch tip root radius. The layers were separated and examined by *SEM*. Only the  $0^\circ$  tows have fractured up to three tows away from the notch edge, none of the  $45^\circ$  tows have fractured. The *CDG* failure criterion was proposed based on stable crack growth. *CDG* model were compared with the *PSC*, *ASC* and experiments. The data required for the prediction of notched strength is the unnotched strength and the  $K_C$ . The notched strength/diameter to width ratio shows the *ASC* gives better fit to the data. The *CDG* model is in very good agreement with the experiments and similar results obtained as in the *ASC*.

An experimental study of the crack displacement and mixed failure modes (mode I+II) of graphite/epoxy-plates ( $[0/\pm 45/90]_S$ ), having central cracks at different angles ( $15, 30, 45, 60, 75$  and  $90^\circ$ ) with the loading

axis, was conducted by SEIF and SHAHJAHAN [22]. Symmetric loads cause the crack to open (*COD*, mode I), while skew-symmetric loads lead to forward sliding (*CSD*, mode II). The critical stress intensity factors ( $K_{IC}$ ,  $K_{IIC}$ ) can be determined after measuring the *COD* and *CSD*. The Moiré interferometry technique was used to measure in-plane displacement on flat surfaces. The *COD* and *CSD* was determined. The normal and shear stress on the crack was determined according to the stress transformation equations, damage zone and stress reduction ratio was calculated using the *ASC*. The  $K_{IC}$  and  $K_{IIC}$  can be expressed by the  $(COD)_C$ ,  $(CSD)_C$ , Young modulus and crack geometry. The  $K_C$  for the laminate was determined by an empirical approach. The stresses for the orthotropic material were determined according to *LEFM* using the stress intensity factors. When fracture occurs, at low angle the *CSD* is higher than the *COD*, increasing the angle *COD* becomes higher than *CSD*. The experimental and *LEFM* results for the normalized critical stress intensity factors show very good agreement. Results confirmed the applicability of *LEFM*, *COD* and *CSD* as fracture criterion for this material.

## 6 CONCLUSIONS

The fracture toughness is not a material property, but can be used to characterize the fracture behavior of composite materials under varied conditions. Several methods were developed by designers. Beam theory can be applied to obtain closed form equations for the fracture toughness. These equations can be used only in *UD* beam shaped specimens (*ENF*, *SCB*, etc.), and generally have to be completed by various factors to approach the experiments. The compliance of specimens with different shape (*CT*, *SEN*, *VIC*, etc.) and different structure (e.g: woven-fabric) can be determined by the area method or by fitting the experimentally measured compliance. The fracture toughness can be determined numerically by many ways (*MVCCT*, *MCCI*, etc.). The fracture toughness can be affected by many parameters. Tests can be conducted by using wide range of specimen types, e.g. specimens with woven fabric structure, *IPCs*, varied particle or fiber-volume fraction, different fiber orientation, and different specimen configuration. The composites combined with metal laminates can be used to improve the fracture toughness. The specimens always contains a crack, notch or hole, which acts as an artificial starting defect. Crack propagation can be expected in the starting defect. The shape, length and width of the crack can be different. There are a lot of facilities to vary the extrinsic test conditions. The effect of displacement rate varies in wide range, and different behavior can be observed for different materials. The tests conducted at cryogenic and elevated temperature or elevated pressure facilitates to investigate the composites under practical conditions. During the test several type of failure prior to delamination fracture can occur. These effects can decrease or increase the fracture toughness. Numerous authors confirmed *R-curve* behavior. The *R-curve* behavior or stable crack growth are not likely to be realized in real applications, because stable crack growth is only attainable under pure displacement control conditions and such conditions do not exist in practice. In this study publications about the fracture toughness of composites were reviewed to summarize current results and further design trends.



## 7 NOMENCLATURE

1PB	One-point bending	LVDT	Linear variable displacement transducer
3PB	Three-point bending	LVDT*	Linear variable differential transformer
4ENF	Four-point bend end-notched flexure	LVI	Low velocity impact
4PB	Four-point bending	MAPP	Maleic-anhydride-polypropylene
5PB	Five-point bending	MCC	Modified compliance calibration
$Al_2O_3 - SiC_w$	Alumina-silicon-carbide-whisker	MCCI	Modified crack closure integral
ASC	Average-stress criterion	MMB	Mixed-mode bending
BN	Boron nitride	MMF	Mixed-mode flexure
CC	Carbon/carbon composite	MVCCT	Modified virtual-crack-closure-technique
CDG	Critical damage growth	OM	Optical microscopy
CFRML	Carbon-fiber-reinforced metal laminate	PEEK	Polyether ether ketone
CLS	Cracked-lap shear	PP	Polypropylene
CMOD	Crack-mouth opening displacement	PSC	Point-stress criterion
COD	Crack opening displacement	PYFM	Post-yield fracture mechanism
CP-CC	Cross-ply carbon/carbon composite	QI-CC	Quasi-isotropic carbon/carbon composite
CPT	Classical plate theory	QI	Quasi-isotropic
CSD	Crack shearing displacement	RB	Reaction-bonded
CT	Compact tensile	RPP	Recycled polypropylene
C-VE	C-glass fiber/bisphenol-vinylester resin	RT	Room temperature
DCB	Double-cantilever beam	SC	Surface-cracked
DEN	Double-edge-notched	SCB	Single cantilever beam
DENF	Double-end-notched flexure	SEM	Scanning electron microscopy
EB	Energy balance	SEN	Single-edge notched
E-ER	E-glass fiber/bisphenol-epoxy resin	SENB	Single-edge-notched beam
ELS	End-loaded split	SENT	Single-edge notched tensile
ENF	End-notched flexure	SEVNB	Single-edge V-notched bend
E-VE	E-glass fiber/bisphenol-vinylester resin	SHPB	Split Hopkinson pressure bar
FEA	Finite element analysis	Si3N4	Silicon nitride
FE	Finite element	TM	Travelling microscope
FML	Fibre/metal laminates	UD	Unidirectional
FM	Fibrous monolith	VCCT	Virtual-crack-closure technique
GFPP	Glass-fibre-reinforced polypropylene	$V_f$	Fiber-volume fraction
GRP, GFRP	Glass-fibre-reinforced plastic composite	VIC	Vickers indentation crack
ILSS	Interlaminar shear strength	$V_p$	Particle-volume fraction
IPC	Interpenetrating phase composite	WIF	Wedge-insert-fracture
IS	Indentation strength	WOF	Work of fracture
LEFM	Linear elastic fracture mechanics		

## References

- [1] ALLIX O., LEVEQUE D., PERRET L. Identification and forecast of delamination in composite laminates by an interlaminar interface model. *Composites Science and Technology* 1998;58;671-678
- [2] BAZHENOV S.L. Longitudinal splitting in unidirectional fibre-reinforced composites with can open hole. *Composites Science and Technology* 1998;58;83-89
- [3] BELMONTE H.M.S., MANGER C.I.C., OGIN S.L., SMITH P.A., LEWIN R. Characterization and modelling of the notched tensile fracture of woven quasi-isotropic GFRP laminates. *Composites Science and Technology* 2001;61;585-597
- [4] CELEMIN J.A., LLORCA J. The embrittlement of Nicalon/alumina composites at intermediate and elevated temperatures. *Composites Science and Technology* 2000;60;1067-1076
- [5] COLLIN M.I.K., ROWCLIFFE D.J. Influence of thermal conductivity and fracture toughness on the thermal shock resistance of alumina- silicon-carbide-whisker composites. *Journal of the American Ceramic Society* 2001;84;1334-1340

- [6] COMPSTON P., JAR P.-Y.-B., BURCHILL P.J., TAKAHASHI K. The effect of matrix toughness and loading rate on the mode-II interlaminar fracture toughness of glass-fibre/vinyl-ester composites. *Composites Science and Technology* 2001;61;321-333
- [7] DAHLEN C., SPRINGER G.S. Delamination in composites under cyclic loads. *Journal of Composite Materials* 1994;28;732-781
- [8] DUBOIS F., KEUNINGS R. *DCB* testing of thermoplastic composites: a non-linear micro-macro numerical analysis. *Composites Science and Technology* 1997;57;437-450
- [9] FILATOWS G.J., SADLER R.L., EL-SHIEKH A.H.M. Fracture behavior of 3-D braid graphite/epoxy composite. *Journal of Composite Materials* 1994;28;526-542
- [10] FRACASSO R., RINK M., PAVAN A., FRASSINE R. The effects of strain-rate and temperature on the interlaminar fracture toughness of interleaved PEEK/CF composites. *Composites Science and Technology* 2001;61;57-63
- [11] GOTO K., HATTA H. Effect of shear damage on the fracture behavior of carbon-carbon composites. *Journal of the American Ceramic Society* 2001;84;1327-1333
- [12] KAWADA H., SRIVASTAVA V.K. The effect of an acidic stress environment on the stress-intensity factor for *GRP* laminates. *Composites Science and Technology* 2001;61;1109-1114
- [13] KENANE M., BENZEGGAGH M.L. Mixed-mode delamination fracture toughness of unidirectional glass/epoxy composites under fatigue loading. *Composites Science and Technology* 1997;57;597-605
- [14] KUSAKA T., HOJO M., MAI Y.-W., KUROKAWA T., NOJIMA T., OCHIAI S. Rate dependence of mode I fracture behaviour in carbon-fibre/epoxy composite laminates. *Composites Science and Technology* 1998;58;591-602
- [15] LAWCOCK G., YE L., MAI Y.-W., SUN C.-T. The effect of adhesive bonding between aluminium and composite prepreg on the mechanical properties of carbon-fiber-reinforced metal laminates. *Composites Science and Technology* 1997;57;35-45
- [16] LI T.Q., LI R.K.Y. A fracture mechanics study of polypropylene-wood flours blends. *Polymer-Plastics Technology Engineering* 2001;40;1-21
- [17] MCNULTY J.C., BEGLEY M.R., ZOK F.W. In-plane fracture resistance of a crossply fibrous monolith. *Journal of the American Ceramic Society* 2001;84;367-375
- [18] MILLER T.C., LIU C.T. Pressure effects and fracture of a rubbery particulate composite. *Experimental Mechanics* 2001;41;254-259
- [19] MUKHERJE Y.X., GULRAJANI S.N., MUKHERJE S., NETRAVALI A.N. A numerical and experimental study of delaminated layered composites. *Journal of Composite Materials* 1994;28;837-870
- [20] REYES G., CANTWELL W.J. The mechanical properties of fibre-metal laminates based on glass fibre reinforced polypropylene. *Composites Science and Technology* 2000;60;1085-1094
- [21] SCHUEKER C., DAVIDSON B.D. Evaluation of the accuracy of the four-point bend end-notched flexure test for mode II delamination toughness determination. *Composites Science and Technology* 2000;60;2137-2146
- [22] SEIF M. A., SHAHJAHAN M. Mixed-mode failure of graphite/epoxy composites. *Journal of Engineering Materials and Technology* 2001;123;371-377
- [23] SHEN F., LEE K.H., TAY T.E. Modeling delamination growth in laminated composites. *Composites Science and Technology* 2001;61;1239-1251
- [24] SHINDO Y., HORIGUCHI K., WANG R., KUDO H. Double cantilever beam measurement and finite element analysis of cryogenic mode I interlaminar fracture toughness of glass-cloth/epoxy laminates. *Journal of Engineering Materials and Technology* 2001;123;191-197

- [25] S. JOSE, R RAMESH KUMAR, M. K. JANA, G. VENKATESWARA RAO. Intralaminar fracture toughness of a cross-ply laminate and its constituent sub-laminates. *Composites Science and Technology* 2001;61;1115-1122
- [26] SKIRL S., KRAUSE R., WIEDERHORN S.M., RÖDEL J. Processing and mechanical properties of Al<sub>2</sub>O<sub>3</sub>/Ni<sub>3</sub>Al composites with interpenetrating network microstructure. *Journal of the American Ceramic Society* 2001;84;2034-2040
- [27] TOHGO K., FUKUHARA D., HADANO A. The influence of debonding damage on fracture toughness and crack-tip field in glass- particle-reinforced Nylon 66 composites. *Composites Science and Technology* 2001;61;1005-1016
- [28] TSAI J.L., GUO C., SUN C.T. Dynamic delamination fracture toughness in unidirectional polymeric composites. *Composites Science and Technology* 2001;61;87-94
- [29] WANG C., HUANG Y., XIE Z. Improved Resistance to damage of silicon carbide-whisker-reinforced silicon nitride-matrix composites by whisker-oriented alignment. *Journal of the American Ceramic Society* 2001;84;161-164
- [30] WEGNER L.D., GIBSON L.J. The fracture toughness behaviour of interpenetrating phase composites. *International Journal of Mechanical Sciences* 2001;43;1771-1791
- [31] YANG Z., SUN C.T. Interlaminar fracture toughness of a graphite/epoxy multidirectional composite. *Journal of Engineering Materials and Technology* 2000;122;428-433
- [32] ZHU Q., SHOBU K. High-temperature mechanical properties of SiC-Mo<sub>5</sub>(Si,Al)<sub>3</sub>C composites. *Journal of the American Ceramic Society* 2001;84;413-419